Operation of Spindt-Type, Carbon Nanotube Cold Cathodes in a Hall Effect Thruster Environment

IEPC-2013-348

Lake A. Singh[1], Mitchell L. R. Walker[2]
Georgia Institute of Technology, Atlanta, GA 30332, USA
and
Graham P. Sanborn[3], Stephan P. Turano[4], and W. Jud Ready[5]
Georgia Tech Research Institute, Atlanta, GA 30332, USA

Abstract: Electric propulsion devices for space applications greatly reduce the propellant mass requirements on a spacecraft in comparison to chemical rockets. To date, gridded ion engines and Hall effect thrusters (HETs) rely on thermionic hollow cathodes to supply electrons for propellant ionization and ion beam neutralization. Hollow cathodes consume up to 10% of the total propellant used in low-power HET propulsion systems; however, such propellant usage does not contribute to thrust generation. An array of Spindt-type, carbon nanotube cold cathodes that emit electrons through field emission can potentially neutralize the ion beam without consuming any propellant. This work examines the effects that the plasma environment near an operating 200-W BHT-200 HET has on carbon nanotube cold cathodes placed around the circumference of the thruster at the exit plane. For this work, the thruster was operated at the 200 V, 1.05 A operating condition with a facility operating condition of 1.1×10^{-6} Torr-Xe. The physical structures that enable field emission appear largely unaffected by placement in the plasma as well as operation in the plasma. This indicates that a refined design of this carbon nanotube cold cathode could be an alternative to the thermionic cathode used on contemporary low-power HETs.

I. INTRODUCTION

Hall effect thrusters (HETs) have been used for several decades on space vehicles for station keeping and orbital maneuvering [1]. HETs ionize and accelerate propellant electrostatically to generate a high-velocity beam of ions. The HET requires a cathode to supply electrons for propellant ionization and to neutralize the resultant ion beam to prevent spacecraft charging.

The present state-of-the-art cathode used in HETs is the thermionic or hollow cathode, which emits electrons from a heated surface. Thermionic cathodes ionize propellant to amplify the number of electrons extracted from the cathode in order to achieve the emission current required for HET operation. The cathode propellant flow is not accelerated by the thruster to contribute to the thrust. The hollow cathode discharge current does not scale well to low power levels, where it may consume as much as 10% of the total propellant required by the thruster [2]. In contrast, field emission (FE) cathodes do not

---

[1] Graduate Research Assistant, School of Aerospace Engineering, lake1@gatech.edu
[2] Associate Professor, School of Aerospace Engineering, mitchell.walker@ae.gatech.edu
[3] Graduate Research Assistant, School of Materials Science and Engineering and, Georgia Institute of Technology, and Georgia Tech Research Institute, graham.sanborn@gtri.gatech.edu
[4] Research Engineer, Georgia Tech Research Institute, stephan.turano@gtri.gatech.edu
[5] Senior Research Engineer, Georgia Tech Research Institute; Adjunct Professor, School of Materials Science and Engineering, Georgia Institute of Technology, jud.ready@gtri.gatech.edu

consume propellant. The primary consequence of this is up to a 10% increase in system specific impulse of the propulsion system. A secondary consequence is a reduction in the propulsion system power requirements by reducing the power the cathode consumes. This reduction in power is enabling for low-power mission applications, such as Cubesats. In this work, we examine the effects of the HET plume environment on Spindt-type, carbon nanotube cold cathode (CNCC) technology to evaluate their potential as an alternative to the thermionic cathode on low-power HETs.

A. Carbon Nanotube Field Emission

FE is a fundamentally different phenomenon of electron emission from a material compared with the thermionic emission employed in present state-of-the-art hollow cathodes. Thermionic electron emission overcomes the potential barrier of the electronic structure of the material by supplying sufficient thermal energy to the electrons [3]. In contrast, FE overcomes the potential barrier by utilizing an electric field on the order of $10\text{-}10^2$ V/µm to lower the potential barrier enough such that the probability of electrons to quantum mechanically tunnel through the barrier becomes significant [4]. FE is achievable at room temperatures, but the high electric fields required to realize emission leads to geometry and material selection considerations that dominate the design space.

The high electric fields required for FE can be attained via a combination of large potential differences and small spacing. In the limit of minimizing both the potential and the size of the device, electrode spacing is taken to the microscopic level, and the large electric fields are realized through geometric factors.

Normally, large electric fields (>100 V/µm) are needed for FE [5], but this field is highly dependent on the electron source geometry, where sharp tips enhance the macroscopic electric field. These FE sources can be much more efficient and reliable if emission can be achieved at a sufficiently low potential; such systems would provide a marked improvement over current technologies [6-8]. Conductive, high aspect ratio nanomaterials, such as carbon nanotubes (CNTs), have this favorable geometry for improving FE performance by field enhancement. CNTs are ideal for FE by having very high electrical conductivity, high temperature stability, chemical inertness, and a nanoscale, high aspect ratio [9-11].

The seminal work in this type of FE design is attributed to Spindt in 1968, and cathodes of this type are typically referred to as Spindt FE cathodes [12]. Spindt cathodes incorporate arrays of emission tips with an internal gate electrode using silicon microfabrication techniques. Spindt FE tips were historically metal cones whose tips are a few hundred nanometers in diameter and recessed underneath the gate electrode. An electric potential between the FE tips and the gate electrode produces the high electric field necessary to enable FE from the tips. The Spindt design attains high current densities by tightly packing a large number of electrostatically isolated emitting elements [13].

The metal cones used in traditional Spindt cathodes have drawbacks that are not shared by CNTs. As the tips of the metal cones erode from use, the tips blunt and no longer emit as efficiently because their field enhancement factor declines. The metal tips can also interact chemically with the ambient environment, which can change the electronic structure of the emitting material and inhibit further emission. A HET plasma environment also subjects the metal tips of Spindt cathodes to sputtering from the plasma, which can permanently degrade their performance at a rate that far exceeds the degradation of the thruster [14]. In contrast, carbon has a much lower sputtering rate than the metals used for traditional Spindt cathodes [15]. The bond structure of the CNT makes them far less reactive than metal.[9]. Additionally, CNTs do not suffer from erosion performance degradation as a result of their whisker like geometry, which does not experience appreciable tip blunting from erosion.

B. Carbon Nanotube Cold Cathode Design

The details of the CNT electron source specifically designed to prevent shorting of the gate layer has been reported elsewhere [16]. In this design, etch pits extend into the Si substrate, and isotropic

etching is utilized to create a vertical and lateral buffer zone between the gate and CNTs, respectively. Doped silicon serves as the substrate and cathode contact [16]. Thermally-grown SiO_2 about 2 µm thick is used as the insulator, and 500-nm thick doped polycrystalline silicon (p-Si) is used as the gate [16]. Fig. 1 shows a schematic of the fabrication process. Standard ultraviolet lithography is used to pattern the substrate (Fig. 1c). Arrays of 4-µm diameter circles across an 8.5x8.5 mm square with a 50, 100, or 200-µm pitch are patterned on each die.

A Bosch etch process anisotropically etches the p-Si gate (Fig. 1d), and the SiO_2 is isotropically etched in a buffered oxide etch (BOE) solution (Fig. 1e). A second Bosch etch is used to deepen the etch pits by etching into the Si substrate (Fig. 1f). An SF_6 reactive ion etch (RIE) process simultaneously removes the undercut p-Si and increases the diameter of the Si pit (Fig. 1g). The etch geometry allows for electron beam evaporation of the Fe catalyst directly on the base of the pit (Fig. 1h). A low-pressure chemical vapor deposition (LPCVD) system with precisely controlled process parameters is used to produce uniform and consistent CNT growth (Fig. 1j). The LPCVD synthesis uses C_2H_2 and NH_3 or H_2 at 700 °C and 10 mbar for 0.5-5 minutes. The CNT growth can be precisely controlled, remains aligned past the Si pit, and is uniform across many pits [16].

The substrate and CNT structures comprise the "cathode electrode" and are referred to as such throughout this work. This CNCC design field emits when the cathode electrode is biased negatively with respect to the gate electrode.
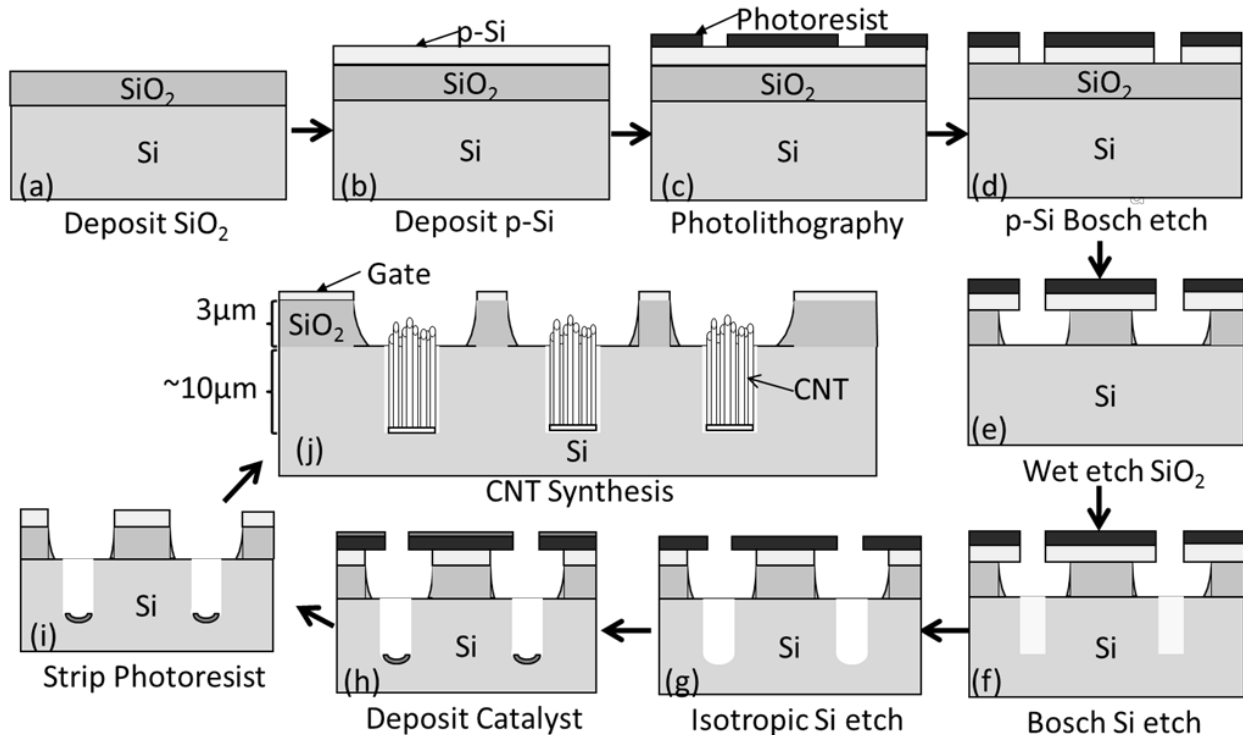

Fig. 1. Fabrication process flow for the internally gated CNT FE design.

II. Experimental Setup

A. Thruster Cathode Array Design

A Kyocera gold-plated, plug-in, hybrid bathtub-type package provides the interface between the CNCC and the rest of the test circuit. Each package is cut in half to reduce its footprint. Fig. 2 shows one CNCC installed on a package. Ablebond 84-ILMI heat cure silver epoxy binds the cathode to the base of

the package, which establishes the electrical and mechanical connection between the package base and cathode. Wire bonds form high-quality (< 1 Ω) connections between the package and the chip by redundantly connecting package pins to the gate on the CNCC and the package base.
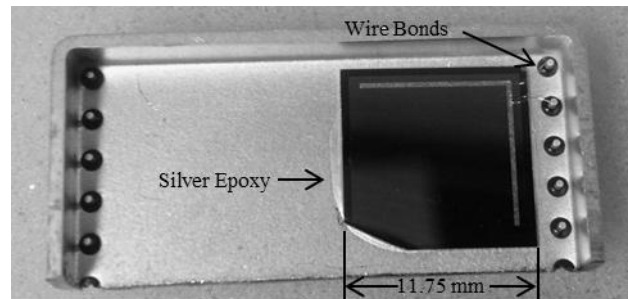

Fig. 2. A CNCC emitter chip installed onto a package with silver epoxy.

The thruster cathode array mechanically and electrically integrates up to 80 packages of CNCCs into a single device for reliable interface to the HET and experimental setup. Fig. 3 shows an exploded view of the array design and Fig. 4 shows the constructed array. The rigid, detachable array can be reused on subsequent experiments, can survive the near-thruster plasma environment, and is light enough to not require additional support when fixed to the HET.

Four identical circuit boards in the array can each accommodate 20 packages. The circuit boards connect all gate electrodes on the installed CNCCs to a common ground plane on the bottom layer of the board and connect each cathode electrode to an independent pin on a DB-25 connection installed on the board. All connections are made through the package pins. A 3/16" machined aluminum back plate provides mechanical support for the circuit boards and forms the base of the array. The side of the aluminum plate interfacing with the circuit boards electrically connects to the ground plane on the bottom of the boards. Channels cut into this side of the plate ensure that the circuit boards mount flush against the plate without undesirable electrical connections with the solder connections on the boards. The opposing side of the plate is Type II anodized at 0.001" thickness to prevent interference from the plasma environment around the thruster.
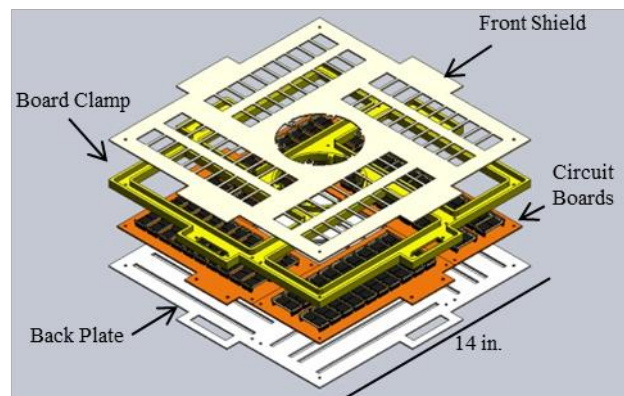

Fig. 3. Exploded view of the thruster cathode array design. The four major components of the array are visible in this view.

A machined G-10 plate (the board clamp) rests on the opposite side of the circuit boards from the back plate and mechanically secures the circuit boards to the back plate. It also provides space between the circuit board surface and an anodized aluminum front shield that obscures sensitive parts of the array from the plasma environment near the thruster. The thruster cathode array interfaces with a Busek BHT-200 200-W HET via the six-radially arranged bolt holes located in the center of the array [17]. Alumina

4

spacers installed in the face of the HET electrically isolate to greater than 10 MΩ the thruster cathode array from the HET during operation.

Fig. 4 shows the placement of 41 CNCCs in the thruster cathode array. All but one CNCC were positioned in the furthest radial locations from the HET to capture the effects of the plume on the CNCCs and minimize the risk of damaging them. Two of the cathodes were included despite exhibiting a short between their cathode and gate immediately after CNT growth. One of the nonfunctional cathodes was positioned in the closest radial position (the proximal sample) and the other was positioned in the furthest radial position (the distal sample) to determine the effects of the plasma on a nonfunctioning CNCC. Both nonfunctional CNCCs were imaged under SEM prior to installation in a repeatable way so that identical emission features could be observed both before and after exposure to the HET plasma.
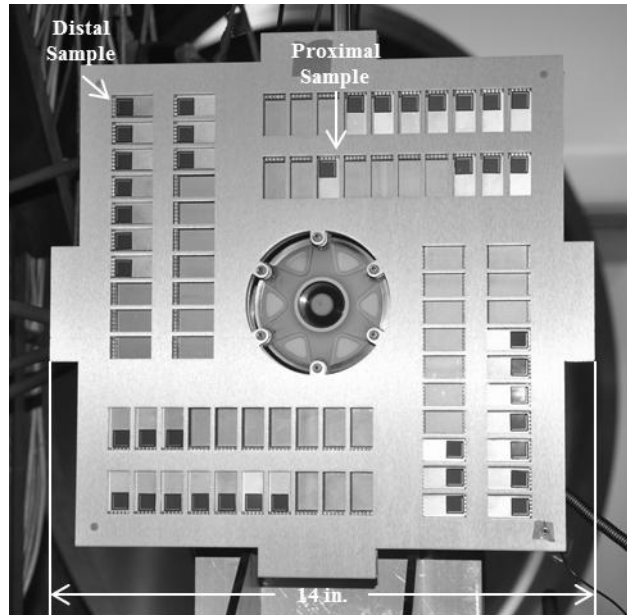

Fig. 4. Thruster cathode array with CNCCs installed and integrated onto a BHT-200 HET. The hollow cathode is located beyond the upper border of the image.

B. Test Circuitry

The data acquisition system developed for this work biases the cathode electrodes in parallel via a common power supply. Each independent cathode channel includes a current shunt and switch to isolate failed or defective CNCCs from the rest of the circuit. A National Instruments PXI-1033 data acquisition chassis equipped with 2 PXI-2567 external relay driver modules, 2 PXI-2527 multiplexer modules, and one PXI-4065 digital multimeter module gathers the data from each of the current shunts during testing. The system records data once every 15 seconds with an accuracy of ± 1μA for current and ± 0.5 V for source potential.

The test circuit shown in Fig. 5 integrates the standard HET circuit with a thermionic hollow cathode and the thruster cathode array test circuit. The discharge power supply energizes the anode of the HET. A second power supply termed "HET Coil" supplies current to generate the magnetic field needed for HET operation. Sharing the discharge low potential with the discharge power supply for the HET, the hollow cathode heater and keeper power supplies drive the operation of the thermionic cathode. The low side of the HET circuit connects to the cathode electrode side of the thruster cathode array circuit in order to make the connection between the two sub-circuits. Between the CNCC power supply and the cathode electrodes lies a component titled "Array Switchboard" which serves to isolate each cathode electrode onto its own parallel circuit and measure current. The National Instruments data acquisition unit interfaces with the Array Switchboard to control the array and acquire the measured current data.
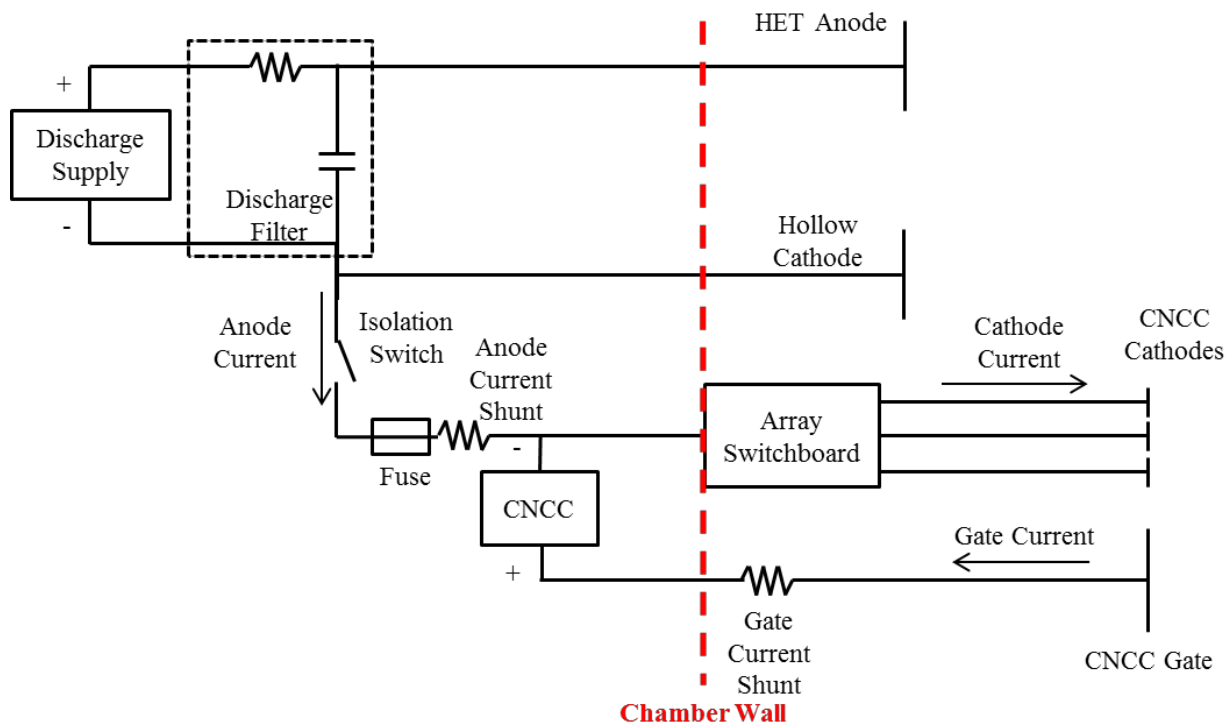
Fig. 5. Full HET test circuit. The HET circuit (top portion) connects to the CNCC circuit (bottom portion) via the HET discharge negative line.

Some additional components added into the circuit protect thruster cathode array components from HET transients during operation. The first protective measure is a normally-open isolation switch. It is closed once the HET is operating in steady-state and the test is ready to begin. The second line of defense is a 315 mA fuse that fails if an overcurrent condition develops in the HET circuit. Previous publications detail the standard triode mode of operation of the CNCC devices [16]. In this circuit configuration, the gate electrode is biased positively with respect to the cathode electrodes, which float at the HET negative discharge potential. The anode of the HET serves as the anode electrode component for the triode configuration, and is biased above both the gate and cathode electrodes. Positive cathode current is defined to be electrons emitting from the electrode, whereas positive gate current is defined to be electrons arriving to the electrode. Positive anode current is defined to be electrons arriving at the anode of the HET, signified by electrons traveling from the HET sub-circuit to the CNCC sub-circuit.

Also visible in Fig. 5 is a UV photodesorption system. An 18-W lamp placed 0.75 m away from the array desorbs gaseous species from the CNT walls and tips prior to initial operation inside the vacuum chamber. The VTF-2 facility at the Georgia Tech High-Power Electric Propulsion Laboratory houses the experiment and produces a base pressure of $1x10^{-9}$ Torr before HET operation begins. The chamber maintains a pressure of $1.1x10^{-6}$ Torr-Xe near the chamber wall during HET operation.

C. Vacuum Facility

This experiment was performed in the Vacuum Test Facility 2 (VTF-2) at HPEPL shown in Fig. 6. VTF-2 is 9.2 meters long and 4.9 meters in diameter. One 3800 CFM blower and one 495 CFM rotary-vane pump bring the system to vacuum. Ten liquid nitrogen cooled CVI TMI re-entrant cryopumps with a combined pumping speed of 350,000 l/s on xenon bring the chamber to a base pressure of 8.9×10^{-10} Torr. A Stirling Cryogenics SPC-8 RL Special Closed-Looped Nitrogen Liquefaction System supplies liquid nitrogen to the cryopump shrouds. MKS 1179A mass flow controllers meter the propellant and a

constant volume calibration system is used to calibration the mass flow rate. Two ionization gauges, Varian 571 and UHV-24, are mounted on either side of the chamber.
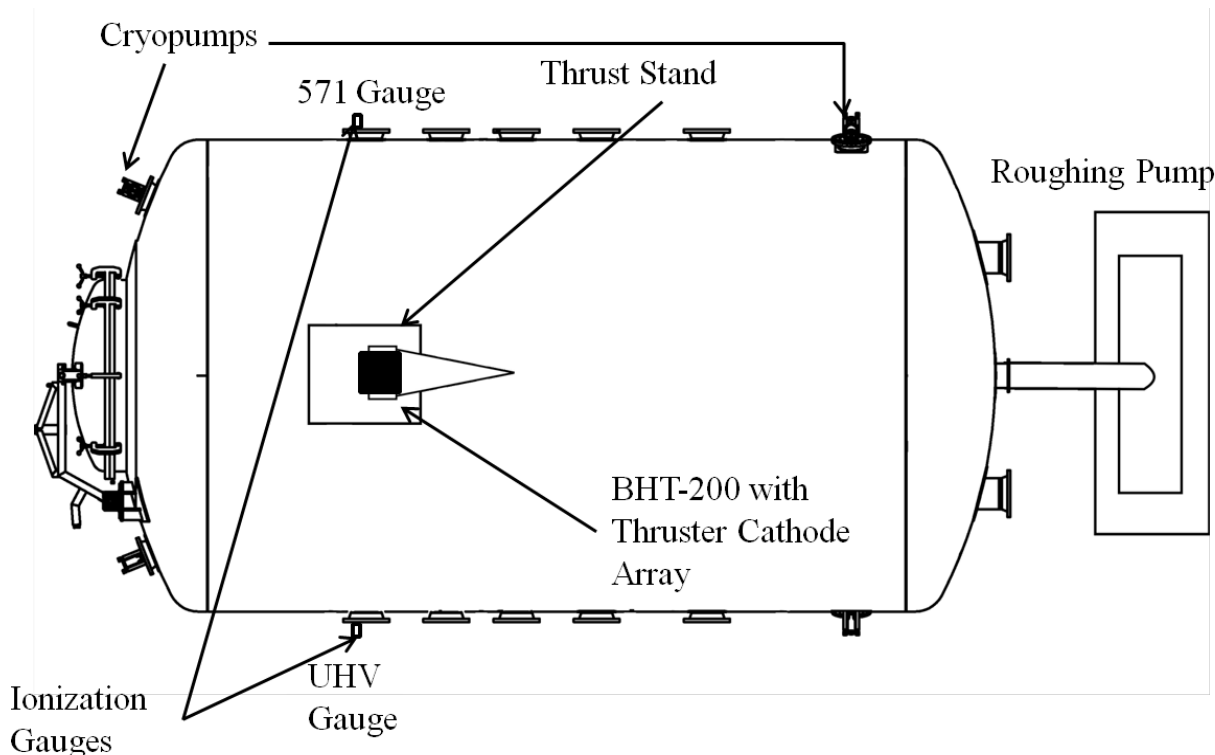

Fig. 6. VTF-2 Vacuum test facility at HPEPL (not to scale)

III. RESULTS AND DISCUSSION

A. **Test Current Data**

Fig. 7 shows the thruster cathode array current and applied potential data as a function of time over the duration of the experiment. The collected data can be broken up into four distinct stages based on how the experiment was conducted. Before data collection, the HET is operated nominally with the hollow cathode. The isolation switch between the HET and CNCC sub-circuits was open during this portion of the experiment. Once the HET operating voltages and currents stabilized, the data acquisition program began capturing data and the isolation switch was closed. This integrated the CNCC sub-circuit into the HET sub-circuit. The data acquisition system measured baseline data for the circuit with the CNCCs unbiased for 2 minutes before biasing the CNCCs. Once the CNCCs were biased, the system operated for five minutes before all CNCCs appeared to be shorted between their cathode and gate electrodes. Data acquisition ended at this point. The entire test sequence occurred during 40 minutes of HET operation. The test was concluded at 40 minutes in case the HET plasma was causing damage to the CNCCs.

The first stage covers the first two data points. The switch connecting the HET and CNCC circuits is open during this stage. Consequently, no current travels between the CNCC circuit and HET circuit (stated as anode current). There are 68-200 μA of gate and cathode current during this period. The HET was already running at steady-state at the beginning of the test, so the current is likely noise from the charge exchange (CEX) ion and hollow cathode electron collisions.

The second stage consists of the next 9 data points. The switch isolating the CNCC and HET circuits is closed at the beginning of this stage, but the CNCC power supply has not started outputting.

7

Power supply output starts during the middle of the second stage, as seen by the small jump in gate voltage from 0 V to 0.575 V at 1.5 minutes. Negative gate current, positive anode current, and positive cathode current result from closing the switch. The currents detected correspond with CEX ions bombarding the CNCC surfaces, which are now set to the negative discharge potential on the HET circuit.

The third stage consists of the large positive plateau, where the experiment software interpreted the currents detected as the trigger to initiate a current-controlled test. At this point, the gate potential rises to +50 V from the cathode potential, which is equal to the HET discharge negative potential (about -10 V).
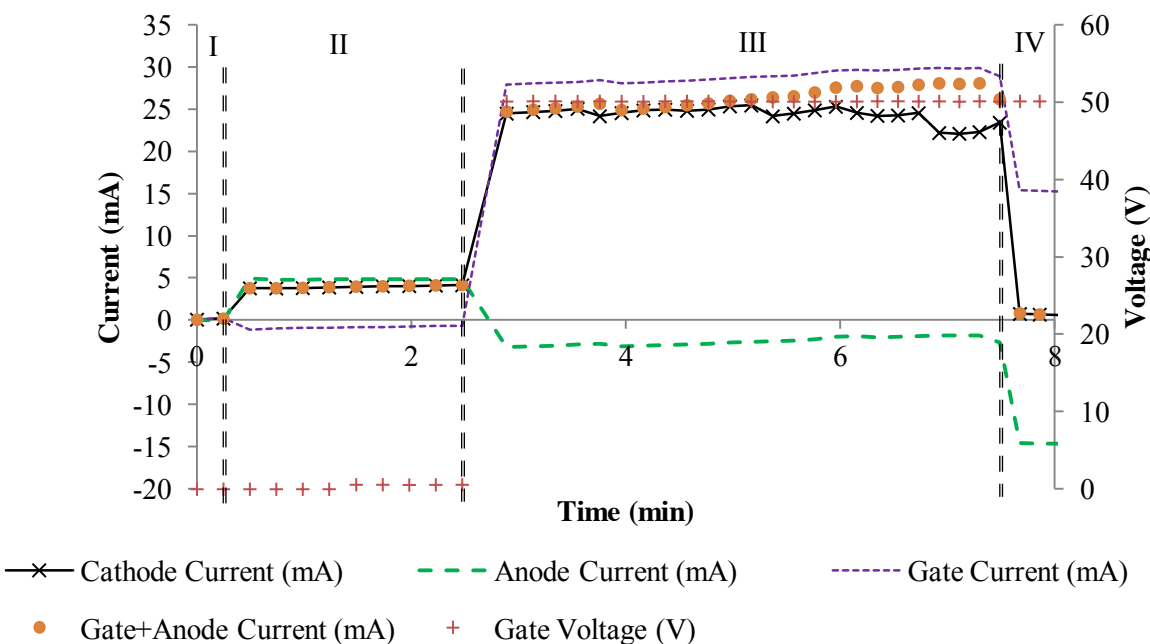

Fig. 7. Full thruster cathode array current data.

A previous publication details typical performance of the CNCC technology used in this work [16] and reveals limited cathode current density (< 50 µA/cm^2) at a bias of 50 V. In contrast, the measured cathode current from this test equates to a current density of roughly 650 µA/cm^2. The order of magnitude difference in documented performance provides evidence that charged particles from the plasma and electrical shorting form the primary contributions to the currents measured. There is a large positive gate current, which corresponds to electrons from the hollow cathode colliding with the positively biased gate. Enough electrons arrive at the gate that they reverse the desired direction of current between the HET and CNCC sub-circuits. This effect is manifested as a negative anode current. There is also positive cathode current, which corresponds with CEX ions colliding with the CNT and exposed package areas seen in Fig. 2. The gate + anode current values diverge from the cathode current because the experiment software stopped acquiring cathode current data on some channels even though they were still active.

The fourth stage consists of three data points. In this stage, the emitter channels are manually shut down. The experiment software experienced an error where it stopped measuring the cathode current on channels without disconnecting them from the cathode bias. This software error was compounded by a circuit flaw that allowed the common gate electrode to be biased by the power supply even when the cathode channel was disconnected. Cathodes on disconnected channels float to the plasma potential, resulting in an electric field which has lower magnitude than that generated by the completed circuit still forming between the cathode and gate electrodes. Since the anode and gate electrodes are common, the current from the disconnected channels is detectable on these electrodes while the data acquisition system

8

does not measure the current from the cathode side of the circuit. These two issues together account for the sharp decline of the gate + anode current and cathode current. They also account for the reduction in discrepancy between the gate + anode current and the cathode current.

B. **Before and After SEM Comparison**

The proximal and distal nonfunctioning CNCC samples underwent repeatable SEM imaging both prior to and after HET exposure. Fig. 8 shows a single emission feature on the distal sample prior to (Fig. 8a) and after (Fig. 8b) the HET test. Close examination reveals the overall structure to be identical between the two images, with two exceptions. One, the post-exposure image shows some particulate debris present in the emission feature marked with arrows. Both the proximal and distal samples have a few features with similar debris accumulation. This particulate debris could be from spallation on part of the array. The debris could also be from handling the devices between the two images when they were unavoidably transported outside of a cleanroom environment for testing.

Two, the before and after images in Fig. 8 show differences in contrast and charging. A difference in contrast could indicate topological changes on the surface, but the difference is most likely attributable to charging of the gate electrode and a change in the accelerating voltage on the SEM. The accelerating voltage is at 1 kV in Fig. 8b as opposed to 10 kV in Fig. 8a because the CNCC is not removed from the electronic package after the test to avoid damage from removal. SEM images from before HET testing were taken without the package. The dummy sample was not wire bonded to the package, which made it very difficult to make a quality contact to the floating gate to ground it during imaging. The poor contact caused significant charging of the gate during imaging, even with a lower accelerating voltage. In addition, the magnetic package (Ni-based Kovar) can cause significant imaging problems due to its interactions with the imaging electron beam. All of the post HET test SEM images in this section contain this variation.
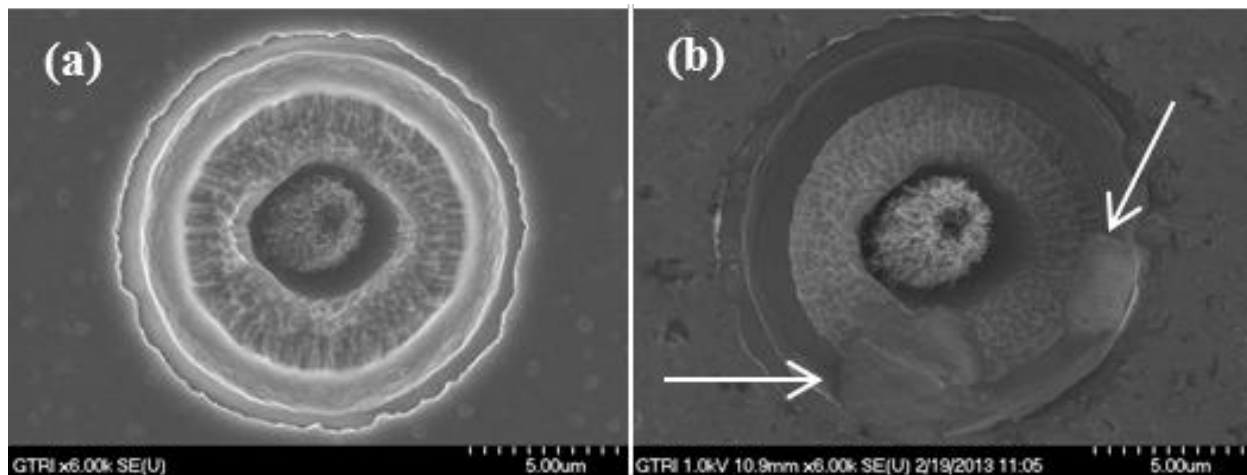

Fig. 8. Before (a) and after (b) SEM images of the same emission feature from the distal sample. Arrows in (b) point to particulate debris present in the feature after exposure to the HET environment.

Fig. 9 shows a fortuitously mis-grown CNT on the poly-silicon surface of the distal sample before (Fig. 9a) and after (Fig. 9b) HET exposure. The position of the CNT remains largely unaffected between the two images, but some changes are present. In particular, the part of the CNT in the upper left of both images appears to have flipped or twisted, while the component of the CNT on the lower right of the image appears to have untwisted and dropped slightly into the nearby etched pit. These changes in position could be due to HET exposure or to handling during the installation and removal of the distal sample from the thruster cathode array. Previous studies report motion of CNTs under the presence of

electric fields and during field emission [18, 19]. While this CNT cannot have performed field emission, it was exposed to the HET plasma and the electric field variations present at its length scale could be responsible for this observed behavior. A more detailed analysis of this effect is beyond the scope of this work.
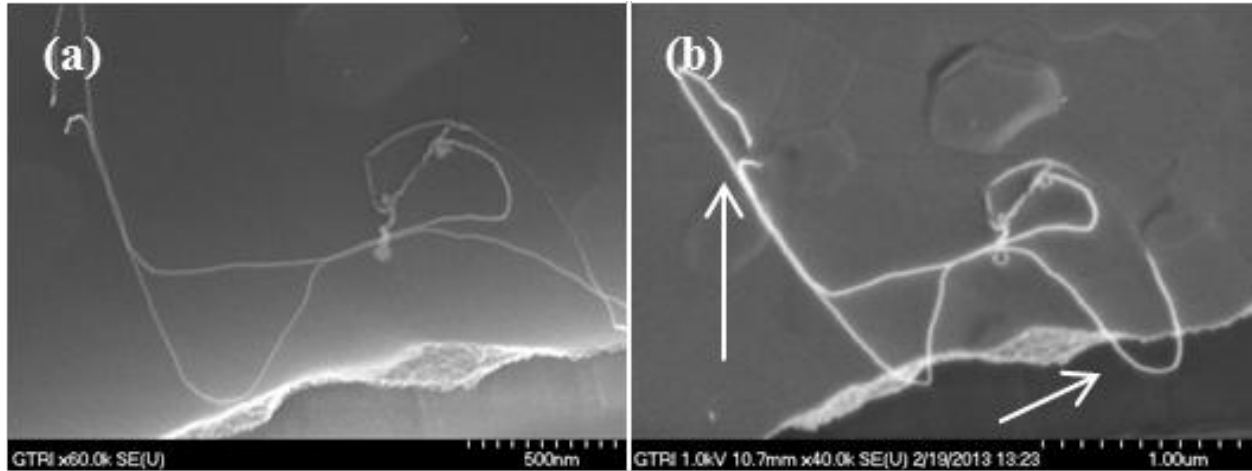

Fig. 9. Before (a) and after (b) images of the same stray CNT on the poly-silicon surface of the distal sample. The CNT has moved slightly between imaging sessions.
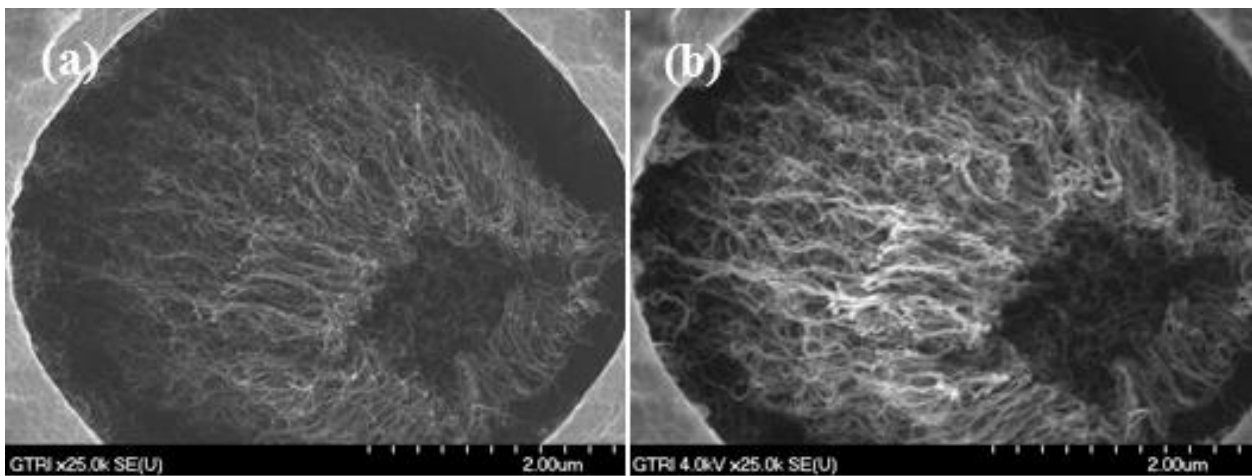

Fig. 10. Before (a) and after (b) images of the same CNT bundle on the proximal sample. The CNT bundle appears to be unaffected by exposure to the HET environment.

Fig. 10 shows a single CNT bundle on the proximal sample before (Fig. 10a) and after (Fig. 10b) HET exposure. Like most emission features on the CNCCs exposed to the HET environment, there are no observable changes in the emitter geometry after exposure. Close examination of these images reveals no observable differences in the poly-silicon gate, the SiO_2 insulator, the silicon substrate, or the CNTs. The remarkable similarity between the two images in Fig. 10 proves that CNCC technology can survive short-term exposure to a near HET environment when not biased and shielded by the gate electrode. Fig. 11 extends this result to functioning, shielded emission features by indicating no damage after exposure to the HET environment when compared with a similar structure in Fig. 8a.
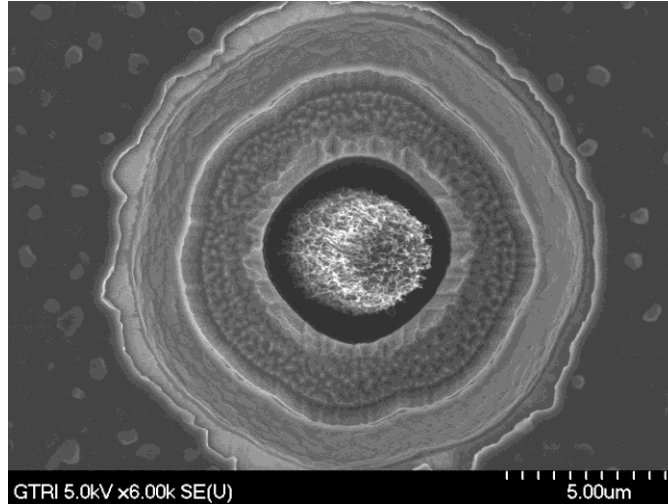
Fig. 11. SEM image of a single emission feature on a CNCC which was biased while inside the HET environment. The emission feature appears undamaged after operation in the HET environment.

C. Arcing and Sputtering

While most emission features on the CNCCs appear unaffected by operation in and exposure to the HET environment, arcing failure between the gate and cathode electrodes observable outside of a HET environment still occurs on some features. Additionally, significant sputtering of the gold plating on the electronic packages resulted in shorts developing on some packages between the package body and gate electrode pins. These shorts are due to the sputtered gold adhering to the insulation between the gate electrode pins and the package body, thus creating an electrically conductive pathway.

The symmetry of the array allows for CNCCs placed in the same slot across different quadrants to be treated together. Fig. 12 maps the number of occurrences of arcing failure and gold sputter failure across the thruster cathode array. Each slot had four packages placed around the array. The number on the top in each slot indicates the number of electronic packages that shorted from sputtered gold, whereas the number on the bottom indicates the number of CNCCs that failed from arcing between the cathode and gate electrodes. In this depiction, the BHT-200 lies beyond the bottom of the image.
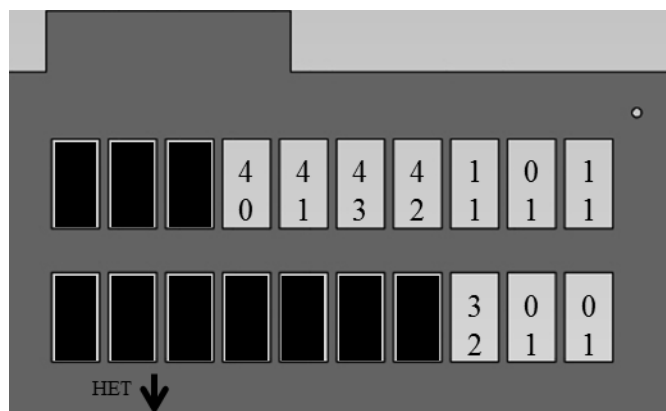

Fig. 12. Schematic of one quadrant of the thruster cathode array. The numbers on the top of each CNCC location indicate the number of packages in this slot around the array that shorted from sputtered gold, whereas the number on the bottom indicates the number of CNCCs that suffered failure from arcing.

Plotting the sputtering short data in this manner reveals a clear transition from packages which shorted due to sputtering at positions close to the HET to packages that did not short due to sputtering far from the HET. Careful examination of the insulation on the electronic packages reveals that all packages experienced sputtering, although some packages did not experience sufficient sputtering to create a conductive pathway. The amount of material sputtered is a function of the incident energy of the ions, the binding energy of the sputtered material, the relative atomic masses, and the number of incident ions [20]. Since significant sputtering occurred on the farthest packages, it is likely that variation in the ion density is responsible for the noted transition. Also of note, the quadrant of the array that was closest to the hollow cathode did not exhibit any observable differences compared with the other three quadrants.

The sputtering varies with distance from the HET as a result of variation in the ion density, but the frequency of arcing failure does not share this variation. This indicates that the variation in the ion density does not significantly alter the likelihood of an arc failure occurring on a CNCC sample.

IV. CONCLUSIONS

This effort is the first experimental study of CNT emitters in an operational HET environment. While field emission from the Spindt-type emitters was undetectable, the experiment yielded valuable insight into the behavior of these devices in the HET environment and highlights design areas for refinement. Emission current data gathered during thruster cathode array operation suggests a significant flow of CEX ions and electrons to the CNCC electrodes. CEX ions that flowed to the array sputtered appreciable amounts of gold from the electronic packages that the CNCC devices were mounted on. Despite this sputtering of gold, there is no evidence of sputtering on the CNCC devices themselves after a total 40-minute exposure to the HET environment. SEM imaging indicates possible spallation from part of the thruster cathode array, but the evidence is more likely an artifact of handling the devices outside of a clean room environment. Some CNTs, which remained unbiased during the test, moved slightly in between the before and after SEM imaging sessions. The motion could be from documented effects of electric field on CNT structures or from handling of the devices. Examination of the locations where different types of failure occurred on the thruster cathode array reveal a positional correlation for sputter-induced short circuiting on the electronic packages, but no positional correlation for arcing failure typical of this CNCC design. A lack of correlation between the two failures implies that the variation in ion density is responsible for the variation in sputtering, but does not affect the likelihood of arcing failure.

The effect of backflow of ions and electrons from the HET and hollow cathode to the thruster cathode array surfaces was more severe than anticipated. A refined design that better shields and insulates the electrodes from the charged species in the plasma will see a dramatic improvement in performance over those CNCCs tested in this work. Future work will include a redesign of the thruster cathode array and extended operation of the CNCC's in the plasma environment near the circumference of the thruster at the exit plane..

REFERENCES

[1]   V. Kim, et al., "Electric Propulsion Activity in Russia," in *International Electric Propulsion Conference*, Pasadena, CA, 2001.
[2]   K. K. Jameson, et al., "Cathode Coupling in Hall Thrusters," in *International Electric Propulsion Conference*, Florence, Italy, 2007.
[3]   W. A. Mackie, P.R. Davis, "Single-crystal zirconium carbide as a high-temperature thermionic cathode material," *IEEE Transactions on Electron Devices*, vol. 36, pp. 220-224, 1989.
[4]   G. A. Vincent, A. Chantre, D. Bois, "Electric field effect on the thermal emission of traps in semiconductor junctions," *Journal of Applied Physics*, vol. 50, pp. 5484-5487, 1979.
[5]   R. Gomer, *Field emission and field ionization*. Cambridge: Harvard University Press, 1961.

[6] W. I. Milne, K. B. K. Teo, G. A. J. Amaratunga, P. Legagneux, L. Gangloff, J. P. Schnell, V. Semet, V. Thien Binh, and O. Groening, "Carbon nanotubes as field emission sources," *Journal of Materials Chemistry,* vol. 14, pp. 933-943, 2004.

[7] J. D. Carey, "Engineering the next generation of large-area displays: prospects and pitfalls," *Philosophical Transactions of the Royal Society London, Series A (Mathematical, Physical and Engineering Sciences),* vol. 361, pp. 2891-907, 2003.

[8] K. J. Lee, "Current limiting of field emitter array cathodes," Ph.D., Materials Engineering, Georgia Institute of Technology, Atlanta, 1986.

[9] A. Loiseau, P. Launois, P. Petit, S. Roche, and J.-P. Salvetat, *Understanding Carbon Nanotubes: from Basics to Applications* vol. 677. Berlin / Heidelberg: Springer, 2006.

[10] W. I. Milne, K. B. K. Teo, M. Chhowalla, G. A. J. Amaratunga, S. B. Lee, D. G. Hasko, H. Ahmed, O. Groening, P. Legagneux, L. Gangloff, J. P. Schnell, G. Pirio, D. Pribat, M. Castignolles, A. Loiseau, V. Semet, and V. Thien Binh, "Electrical and field emission investigation of individual carbon nanotubes from plasma enhanced chemical vapour deposition," *Diamond and Related Materials,* vol. 12, pp. 422-428, 2003.

[11] W. A. de Heer, A. Chatelain, and D. Ugarte, "Carbon nanotube field-emission electron source," *Science,* vol. 270, p. 1179, 1995.

[12] C. A. Spindt, "A Thin Film Field Emission Cathode," *Journal of Applied Physics,* vol. 39, pp. 3504-3505, 1968.

[13] K. J. Lee, "Current limiting of field emitter array cathodes," Ph.D., Materials Engineering, Georgia Institute of Technology, Atlanta, GA, 1986.

[14] C. M. Marrese, et al., "Performance of Field Emission Cathodes in Xenon Electric Propulsion System Environments," in *Micropropulsion for Small Spacecraft.* vol. 187, 1 ed Reston, VA: American Institute of Aeronautics and Astronautics, 2000, pp. 271-302.

[15] W. M. Stacey, *Fusion Plasma Physics.* Darmstadt: Wiley-VCH, 2005.

[16] G. Sanborn, S. Turano, P. Collins, and W. J. Ready, "A thin film triode type carbon nanotube field emission cathode," *Applied Physics A,* pp. 1-6, 2012/10/01 2012.

[17] V. Hruby, et al., "Development of low power Hall thrusters," in *30th Plasmadynamics and Lasers Conference,* Norfolk, VA, 1999.

[18] Z. L. Wang, et al., "In situ imaging of field emission from individual carbon nanotubes and their structural damage," *Applied Physics Letters,* vol. 80, pp. 856-858, 2002.

[19] Y. Saito, K. Seko, J. Kinoshita, "Dynamic behavior of carbon nanotube field emitters observed by in situ transmission electron microscopy," *Diamond and Related Materials,* vol. 14, pp. 1843-1847, 2005.

[20] N. Matsunami, et al., "Energy dependence of the ion-induced sputtering yields of monatomic solids," *Atomic Data and Nuclear Data Tables,* vol. 31, pp. 1-80, 1984.